International Journal of Heat and Mass Transfer 136 (2019) 864–876

Contents lists available at ScienceDirect

International Journal of Heat and Mass Transfer

journal homepage: www.elsevier.com/locate/ijhmt

An experimental study on the thermal effects of duty-cycled plasma actuation pertinent to aircraft icing mitigation

Yang Liu [a], Cem Kolbakir [a], Haiyang Hu [a], Xuanshi Meng [b], Hui Hu [a,*]

[a] Department of Aerospace Engineering, Iowa State University, Ames, IA 50011, USA
[b] Department of Fluid Mechanics, Northwestern Polytechnical University, Xi'an, Shaanxi 710072, China

ARTICLE INFO

Article history:
Received 7 December 2018
Received in revised form 11 March 2019
Accepted 11 March 2019
Available online 15 March 2019

Keywords:
Duty-cycled DBD plasma
Thermal effect
Aircraft icing mitigation

ABSTRACT

An experimental study was performed to evaluate the effectiveness of utilizing the thermal effects induced by duty-cycled dielectric barrier discharge (DBD) plasma actuation for aircraft icing mitigation. The experimental study was carried out in the unique Icing Research Tunnel available at Iowa State University (i.e., ISU-IRT) with a NACA0012 airfoil model embedded with DBD plasma actuators exposed under a typical glaze icing condition. During the experiments, the DBD plasma actuators were operated in two different modes for a comparative study, i.e., in duty-cycled actuation mode vs. in conventional continuous actuation mode as the comparison baseline. While the anti-/de-icing performances of the DBD plasma actuators under different actuation modes were revealed clearly based on the snapshot images acquired by using a high-speed imaging system, an infrared (IR) thermal imaging system was also used to map the corresponding surface temperature distributions over the ice accreting airfoil surface in order to characterize the thermal effects induced by the plasma actuations. It was found that, with the same power input, the plasma actuation in duty-cycled mode would have a higher instantaneous voltage during the "on" periods, resulting in much stronger thermal effects for an improved anti-/de-icing performance, in comparison to the case in the continuous actuation mode. The thermal effects induced by the duty-cycled plasma actuation were found to be further enhanced by increasing of the modulating frequency of the duty cycles, which is a very promising approach to further improve the anti-/de-icing performance of DBD plasma actuation. The findings derived from the present study could be used to explore/optimize design paradigm for the development of novel DBD-plasma-based anti-/de-icing strategies tailored specifically for aircraft icing mitigation.

1. Introduction

Aircraft icing has been widely recognized as a serious weather hazard to aviation safety. When aircraft fly through cloud layers in cold weathers, in-flight icing may occur as the super-cooled water droplets suspended in the cloud freeze over aircraft surfaces upon impacting on airframes [1]. Ice accretion on aircraft surfaces can cause dramatic lift decrease and drag increase of aircraft due to the contamination of streamlined airfoil profiles by the accreted ice shapes [2]. Depending on the environmental parameters and flight conditions, in-flight icing can be either dry or wet, which are termed as rime and glaze [3]. Rime ice usually forms when the ambient temperature is relatively cold (i.e., typically below −10 °C) and the airflow is dry with a lower liquid water content (*LWC*). In such cold and dry conditions, the supercooled water droplets would freeze immediately upon impact on the aircraft surfaces due to the rapid heat transfer which can instantly remove all of the latent heat of fusion released during the solidification process of the impinged water droplets. When the air temperature is warmer, i.e., just below the water freezing temperature, and the *LWC* level in the airflow is relatively high, the impinged supercooled water droplets would only freeze partially due to the insufficient heat transfer to remove all of the latent heat of fusion in the water droplets, allowing the remaining water mass to transport freely over the aircraft surfaces. The ice layer formed in such conditions is found to have complex geometries/structures (e.g., "horns" shaped ice), which is commonly called glaze ice. Although many efforts have been made in recent years to elucidate the underlying physics of aircraft icing [4–8] and develop new techniques to mitigate the icing processes [9–14], aircraft icing remains as an important unsolved problem at the top of the National Transportation Safety Board's most wanted list of aviation safety improvements.

* Corresponding author.
E-mail address: huhui@iastate.edu (H. Hu).

https://doi.org/10.1016/j.ijheatmasstransfer.2019.03.068
0017-9310/

To reduce the harmful effects of aircraft icing, a number of anti/de-icing systems have been developed, including both active and passive approaches. While the active anti-/de-icing methods are mainly dependent on the use of de-icing fluids [15], electro-thermal melting [16] and mechanical/ultrasonic-based surface deformation [14,17], the passive anti-icing strategies are principally developed by using the specialized hydro- and ice-phobic coatings/materials [11,13,18–21]. Though the goal of anti-/de-icing on aircraft has been achieved by using these techniques, they are suffering from various drawbacks. For example, the extensive use of de-icing fluids at airports has caused significant environmental pollutions to soil and water due to the deposition and dissipation of aqueous solutions of propylene and ethylene glycol along with other chemical additives [15]. Mechanical (e.g., pneumatic) and ultrasonic-based anti-/de-icing systems have been used to break off ice chunks accreted on aircraft surfaces, which may pose foreign object damage (FOD) hazards to aero-engines [16]. The hydro- and ice-phobic coatings/materials have been demonstrated to have great icephobicity in static laboratory tests (i.e., by spraying water droplets or pouring water onto substrates, and then froze the test samples in refrigerators). However, these coatings are found to be very unreliable for in-flight icing mitigation (i.e., with high-speed impacts of super-cooled water droplets onto aircraft surfaces) due to their very poor durability attributed to the rapid surface degradation in icing conditions [21,22]. While electro-thermal de-icing systems have been widely used to melt out ice by heating up aircraft surfaces [10,23,24], they are usually very inefficient and have demanding power requirements, and can also cause damage to composite materials from overheating. In looking to achieve better anti-/de-icing efficiencies on aircraft beyond the current icing mitigation methods, technologies with less complexity, power requirement, and adverse environmental impacts are highly desirable.

In recent years, a novel plasma-based anti-/de-icing technique was developed [12] by utilizing the thermal effects induced in surface dielectric barrier discharge (SDBD) plasma actuation (which is a type of discharge producing an ionized gas at the dielectric surface by the application of high amplitude and high frequency of Alternative Current (AC) voltage, i.e., AC-DBD, or nanosecond-scale pulsed voltage, i.e., ns-DBD, between two electrodes separated by a dielectric layer [25]). It has been demonstrated that the DBD plasma actuators have a great potential for more efficient anti-/de-icing operations on aircraft in comparison to the conventional electro-thermal methods [26]. While the conventional electrical film heaters function as anti-/de-icing devices by heating up the surface to melt out the ice accretion, the newly developed plasma-based method is suggested to be able to directly heat up the impinging water droplets as they passing through the heated gas layer close to the airfoil surface [26]. As a widely used flow control method, DBD plasma actuation has drawn extensive attentions in the aerodynamic community over the past decades [27]. Numerous studies have been conducted to improve the efficiency of DBD plasma actuators in separation control and delay/promotion of boundary layer transition [25]. However, only limited work [12,26,28] can be found in literatures to address the thermal effects in DBD plasma actuation and the associated application/optimization for icing mitigation. Further optimization and modification of DBD plasma actuators to maximize the use of thermal energy generated in plasma actuation is highly desirable for the development of more effective plasma-based anti-/de-icing technology designed specifically for aircraft icing mitigation.

Among the many optimization methods of DBD plasma actuation, the duty-cycle control of plasma actuation has been demonstrated to be a very effective way to improve the control efficiency in flow optimization [29–31]. While the steady (continuous) plasma actuation produces an induced flow close to the wall, the duty-cycled plasma actuation could create a train of co-rotating vortices [30]. It has been revealed that the size, shape, and propagation velocity of the vortices generated in the duty-cycled plasma actuation are highly dependent on the duty cycle and pulse frequency [30–33]. It was also found that along with the increase of the duty-cycle frequency of plasma actuation, the generated vortices would become smaller (i.e., more closer to the wall) with more concentrated vorticity [33]. It was suggested that the induced train of vortices in the duty-cycled plasma actuation could significantly promote the mixing of the boundary layer airflow and the mainstream [33]. Since the heat transfer mechanism in plasma actuation is closely coupled with the induced boundary layer airflow, the thermal effect in duty-cycled plasma actuation is therefore suggested to be very different from the steady plasma actuation. However, there is no data available in literatures to address the thermal effects in duty-cycled plasma actuation. The present study aims to reveal the thermal characteristics of duty-cycled plasma actuation to provide guidelines for the further optimizations of plasma-based anti-/de-icing technologies.

In the context that follows, the fabrication and implementation of the DBD plasma actuators for anti-/de-icing applications were introduced first. Then, the mechanisms of modulating the duty-cycled plasma actuation was illustrated. The DBD plasma actuations in both continuous and duty-cycled modes were achieved on a NACA0012 airfoil model to perform a comparative study of the anti-/de-icing performances between the two different modes of DBD plasma actuations. While the anti-/de-icing performances of the DBD plasma actuators under different actuation modes were revealed clearly based on the snapshot images acquired by using a high-speed imaging system, an infrared (IR) thermal imaging system was also used to map the corresponding surface temperature distributions over the ice accreting airfoil surface in order to characterize the thermal effects induced by the plasma actuations. The impacts of the modulating frequency of duty cycles on the thermal effects induced in the duty-cycled DBD plasma actuations and the corresponding anti-/de-icing performances were also revealed.

2. Experimental setup and test model

The ice accretion experiments were performed in the unique Icing Research Tunnel available at Aerospace Engineering Department of Iowa State University (i.e., ISU-IRT). As shown schematically in Fig. 1, ISU-IRT is a multifunctional icing research tunnel with a test section of 2.0 m in length × 0.4 m in width × 0.4 m in height with four side walls being optically transparent. It has a capacity of generating a maximum wind speed of 60 m/s and an airflow temperature down to − 25 °C. An array of 8 pneumatic atomizer/spray nozzles are installed at the entrance of the contraction section of the icing tunnel to inject micro-sized water droplets (10–100 μm in size with MVD ≈ 20 μm) into the airflow. By manipulating the water flow rate through the spray nozzles, the liquid water content (LWC) in the ISU-IRT could be adjusted (i.e., *LWC* ranging from 0.1 g/m^3 to 5.0 g/m^3). In summary, ISU-IRT can be used to simulate atmospheric icing phenomena over a range of icing conditions (i.e., from dry *rime* to extremely wet *glaze* ice conditions) [34,35].

A NACA 0012 airfoil model was used in the present study, which was made of a hard-plastic material and manufactured by using a rapid prototyping machine (i.e., 3-D printing) that builds 3-D models layer-by-layer with a resolution of about 25 μm. The airfoil model has a chord length of c = 150 mm, which spanned the width of the test section of the ISU-IRT. Supported by a stainless-steel rod, the airfoil model was mounted at its quarter-chord and oriented horizontally across the middle of the test section. In the present study, a typical glaze icing condition was generated in

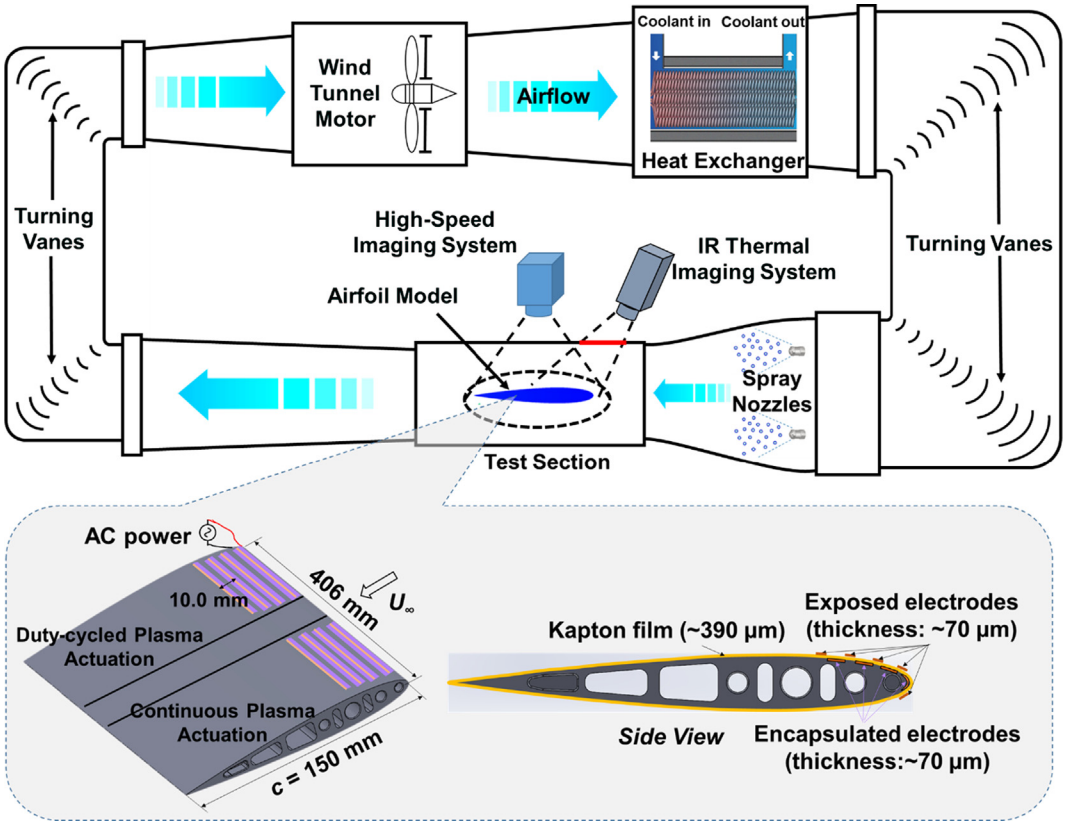

Fig. 1. Schematic of the ISU-IRT and tested airfoil model used in the present study.

the ISU-IRT as described in 14 CFR Part 25 Appendix C [36] (i.e., at the freestream air velocity of U_∞ = 40 m/s, *LWC* = 1.0 g/m^3, and airflow temperature of T_∞ = −5 °C). The angle of attack (α) of the airfoil model was set at α = 0°.

During the experiments, the dynamic ice accretion process over the airfoil surface was recorded by using a high-speed camera (PCO Tech, Dimax) with a 60 mm lens (Nikon, 60 mm Nikkor f/2.8) installed at 500 mm above the airfoil model. The camera was positioned approximately normal to the airfoil chord, with a measurement window size of 210 mm × 210 mm and a spatial resolution of 9.5 pixels/mm. An in-situ calibration procedure as suggested by Soloff et al. [37] was performed to dewarp the captured images before extracting physical features. Each test trial consisted of 3000 images acquired at a frame rate of 10 Hz. As shown in Fig. 1, an infrared (IR) thermal imaging camera (FLIR A615) was also used to map the surface temperature of the ice accreting airfoil surface. The IR camera was mounted at ~300 mm above the airfoil model with the measurement window size of 110 mm × 90 mm and a corresponding spatial resolution of 5.3 pixels/mm. Radiation from the ice accreting airfoil surface will pass through an infrared window (i.e., FLIR IR Window-IRW-4C with optic material of Calcium Fluoride) before reaching to the IR camera. A calibration of the material emissivity is performed for the IR thermal imaging [38]. Table 1 gives the IR emissivity coefficients of the materials relevant to the present study, i.e., surface of the airfoil model, ice, and liquid water, respectively. Each test trial consisted of 15,000 IR images acquired at a frame rate of 50 Hz. An in-situ calibration was also performed to validate the IR thermal imaging results by establishing a relationship between the measured count number from the IR camera and the temperature acquired by using thermocouples. The measurement uncertainty for the IR camera was found to be less than 0.5 °C. The high-speed video camera and the IR camera were connected to a digital delay generator (DDG, Berkeley Nucleonics, model 575) that synchronized the timing between the two systems.

Table 1
Emissivity of the materials pertinent to the test model used in the present study.

Materials	Emissivity
Surface of the airfoil model (Enamel coated)	0.960
Ice	0.965
Water	0.950–0.963

As clearly shown in Fig. 1, a half-half configuration of the DBD plasma actuations (i.e., in the duty-cycled actuation mode *vs.* in the conventional continuous actuation mode) was designed over the airfoil model. Each of the plasma actuators consisted of four encapsulated electrodes and five exposed electrodes, with the same thickness of about 70 μm. In the present study, three layers of Kapton film (i.e., 130 μm for each layer) were integrated to serve as the dielectric barrier to separate the encapsulated electrodes from the exposed electrodes. Ranging from the leading-edge position to about 27% chord length of the airfoil model, four encapsulated electrodes were distributed evenly on both sides along the airfoil model with a separation distance of 3 mm. In the present study, while two sets of exposed electrodes (with length of 96 mm) were fabricated on the two sides of the airfoil model for the continuous plasma actuation and duty-cycled plasma actuation, the same set of encapsulated electrodes with a length of 350 mm was fabricated along the whole span for the plasma actuation on both sides. The width of the encapsulated electrodes was 10.0 mm (except the one at the leading edge which was 5.0 mm). As reported by Liu et al. [35], since most of the ice would be formed around the leading edge of the airfoil model, the width of the first encapsulated electrode was reduced to 5.0 mm in order to generate more plasma near the airfoil leading-edge for a successful anti-/de-icing operation in the region, while the encapsulated

electrodes were attached symmetrically around the leading edge of airfoil. As for the exposed electrodes (i.e., 96 mm in length and 3.0 mm in width), they were placed right above the covered electrodes with zero overlap between the exposed and covered electrodes.

The DBD plasma actuators were wired to a high-voltage AC power supply (Nanjing Suman Co., CTP-2000K), which can provide a maximum 30 kV peak-to-peak sinusoidal voltage with a center frequency of 10 kHz. While the AC current applied to the plasma actuator was measured by using a high response current probe (Pearson Electronics, Inc., Pearson 2877), the high-amplitude voltage was measured by using a high voltage probe (i.e., P6015A from Tektronix), and monitored by an oscilloscope (Tektronix DPO3054). The voltage of the sinusoidal excitation to the electrodes was manipulated with a variable voltage transformer at a constant frequency of 10 kHz. During the experiments, to achieve the duty-cycled plasma actuation, a digital pulse wave generator [32] was used to modulate the carrier AC voltage source with a fixed duty cycle of τ = 50%, which is defined as the fraction of time when the actuator is on over a duty cycle period. Fig. 2 shows a schematic of the modulation from a continuous plasma actuation to a duty-cycled plasma actuation. Various frequencies were modulated for the duty-cycled plasma actuation (i.e., $f_{duty\text{-}cycle}$ = 1, 5, 50, 100, 200 Hz) and were examined in the present study to evaluate the effects of duty cycle frequency on the thermal effects induced in duty-cycled plasma actuation. To quantitatively compare the anti-/de-icing performances of the DBD plasma actuations in the two different modes (i.e., in the duty-cycled actuation mode *vs.* in the conventional continuous actuation mode), the power applied to the plasma actuators were adjusted to be the same throughout the experiments.

3. Results and discussion

3.1. Electrical characteristics of DBD plasma actuation during ice accretion processes

For the use of DBD plasma actuators in anti-/de-icing applications, due to the complex multiphase interactions (i.e., water–ice-air-plasma interactions) occurred in plasma actuation under icing conditions, the electrical characteristics of the plasma actuators were found to be changed before and during the dynamic ice accretion process. Fig. 3 shows an example of the measured voltage and current traces as a function of time within six AC cycles before and during the ice accretion process (i.e., U_∞ = 40 m/s, T_∞ = −5 °C and LWC = 1.0 g/m^3). Before the icing process was started, the plasma discharge over the dielectric surface is in a normal state, which is the same as that reported in the previous studies [39]. As clearly shown in Fig. 3(a), for the plasma discharge without water or ice on the dielectric surface, while the large spikes are observed in the current trace which are caused by the micro-discharges in the plasma area, the voltage trace is found to be kept in a good sinusoidal shape during the plasma actuation.

During the dynamic ice accretion process, since the supercooled water droplets would continuously impinge onto the airfoil surface, the exposed electrodes and the dielectric layer surface were found to be submerged in the water film formed by the impinged water droplets. The surface water film and the further developed water rivulets were suggested to act as conductor extensions of the exposed electrodes in AC-DBD plasma actuation [40]. As a result, the glow discharge in plasma actuation was found to be formed at the edges of the water film/rivulets, rather than the exposed electrodes as usually observed. Fig. 3(b) shows the measured voltage and current traces of the AC-DBD plasma actuator during the dynamic ice accretion process. It can be seen clearly that, while the voltage signal is kept not changed, the amplitude of the large spikes in the current trace is found to be significantly reduced, which is suggested to be caused by the less glow discharge at the running water film/rivulets edges. The power, P, of the plasma actuator in a certain time of duration, T, can be estimated using two methods: electric current method and electric charge method [41]. While the electric charge method applying the nonlinear signal compression circuit was suggested to be more reliable in estimating the power consumption, the electric current method is much more easier to implement and has been widely used in the power calculation of DBD plasma actuation [41]. In the present study, we applied the electric current method to estimate the power (i.e., Eq. (1)) based on the measured voltage and current traces as that shown in Fig. 3.

$$P = \frac{1}{T}\int_0^T V(t)\cdot I(t)dt \tag{1}$$

where $V(t)$ and $I(t)$ are the instantaneous voltage and current applied on the plasma actuator.

For the DBD plasma actuation operated in the conventional continuous mode as shown in Fig. 4(a), since the high-voltage signal is continuously applied to the DBD plasma actuator, the time duration used for the power calculation is usually selected to be

$$T = n_0 R \tag{2}$$

where R is the AC period of plasma actuation, and n_0 is the number of AC cycles. Thus, the power, P_0, of the plasma actuators operated in the continuous mode can be calculated using:

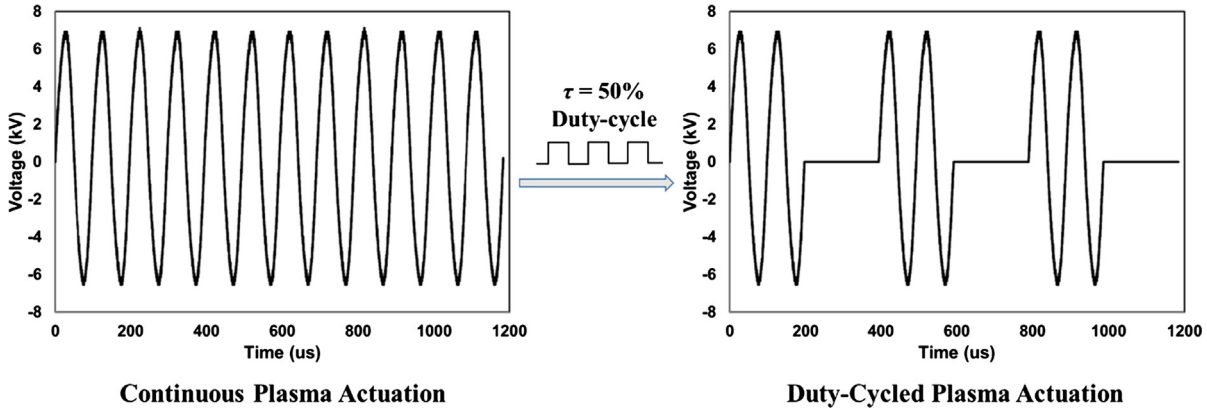

Fig. 2. A schematic of the modulation from a continuous plasma actuation to a duty-cycled plasma actuation.

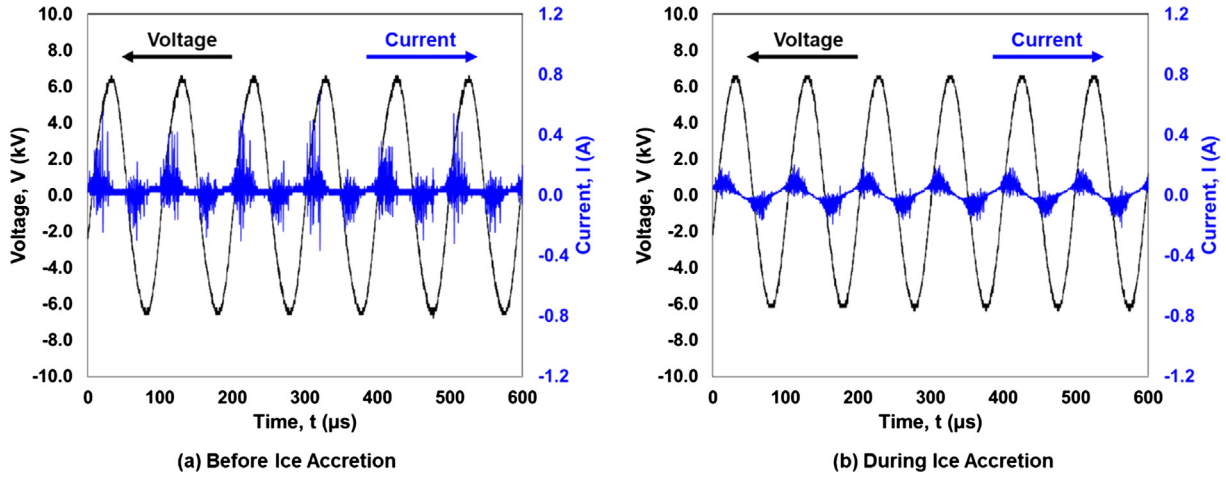

Fig. 3. Measured voltage and current traces of the AC-DBD plasma actuator under continuous mode within six AC cycles before and during the ice accretion process.

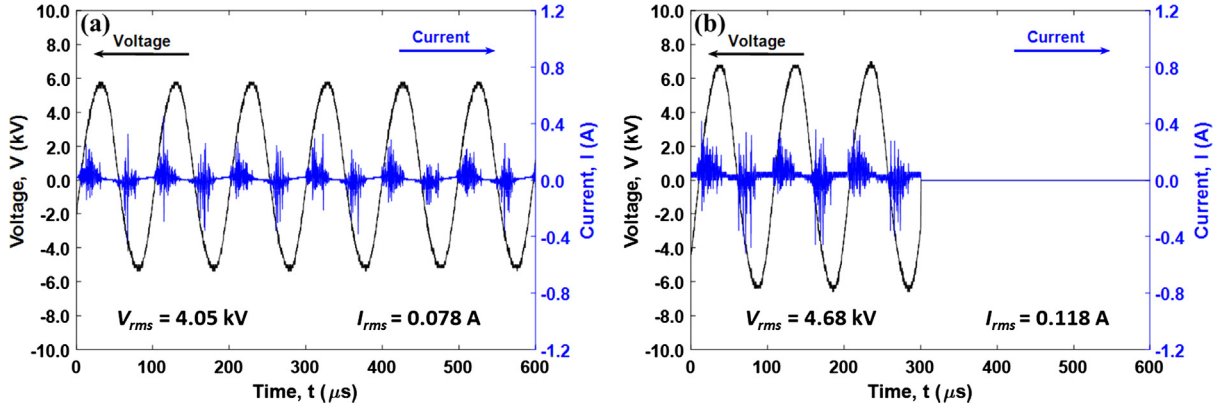

Fig. 4. Measured voltage and current traces of the AC-DBD plasma actuator before ice accretion in (a) the continuous mode and (b) duty-cycled mode (including both "on" and "off" periods of a complete cycle).

$$P_0 = \frac{1}{n_0 R}\int_{n_0 R} V_0(t)\cdot I_0(t)dt \tag{3}$$

where $V_0(t)$ and $I_0(t)$ are the instantaneous voltage and current applied on the plasma actuator.

For the DBD plasma actuation in the duty-cycled mode, however, the voltage and current would be kept at zero periodically during plasma actuation as shown in Fig. 4(b). Depending on the duty cycle of the high-voltage signal, the number of AC cycles in the duty-cycled plasma actuation would be reduced within the same time duration of T, which can be calculated using Eq. (4):

$$n_1 = n_0 \cdot \tau \tag{4}$$

where τ is the applied duty cycle to the input high-voltage signal. As a result, the power, P_1, of the plasma actuators operated in the duty-cycled mode becomes:

$$P_1 = \frac{1}{T}\int_{n_1 R} V_1(t)\cdot I_1(t)dt = \frac{1}{n_0 R}\int_{n_1 R} V_1(t)\cdot I_1(t)dt \tag{5}$$

where $V_1(t)$ and $I_1(t)$ are the instantaneous voltage and current applied on the duty-cycled plasma actuator (when the actuator is "on"). In the present study, since the duty cycle was selected to be τ = 50%, the power of the duty-cycled plasma actuation, P_1 can be calculated as:

$$P_1 = \frac{1}{n_0 R}\int_{\frac{n_0 R}{2}} V_1(t)\cdot I_1(t)dt \tag{6}$$

In order to keep the power the same between the continuous plasma actuation and the duty-cycled plasma actuation, i.e., $P_0 = P_1$, the voltage applied to the DBD plasma actuators would be increased in the duty-cycled mode so that the instantaneous power of the duty-cycled plasma actuator during the "on" periods can be twice of that in the continuous plasma actuation, i.e., $V_1(t)\cdot I_1(t) = 2\,V_0(t)\cdot I_0(t)$. As clearly shown in Fig. 4, in order to have the same power input of $P \approx 40$ W for the anti-/de-icing test in the present study, while the root mean square (RMS) of the input voltage and current in the continuous mode ($V_{0\text{-}p\text{-}p}$ = 11.5 kV) are measured to be $V_{0\text{-}rms}$ = 4.05 kV and $I_{0\text{-}rms}$ = 0.078 A, respectively, the RMS values of the input voltage and current during the "on" period in the duty-cycle mode ($V_{1\text{-}p\text{-}p}$ = 14.0 kV) are measured to be $V_{1\text{-}rms}$ = 4.68 kV and $I_{1\text{-}rms}$ = 0.118 A, respectively.

Based on the measured voltage and current traces of the AC-DBD plasma actuator in the two different modes as given in Fig. 4, both the instantaneous power and the cumulative power of the plasma actuator during the discharge were calculated and shown in Fig. 5. It can be seen clearly that, during the continuous plasma actuation, while the instantaneous power fluctuates along with the alternating positive/negative polarization of the actuator, the cumulative power increases continuously as the time goes by as shown in Fig. 5(a). For the plasma actuation under the duty-cycle mode, it is found that while the cumulative power keeps increasing during the "on" period, the power would be kept not changed during the "off" period. However, due to the increased

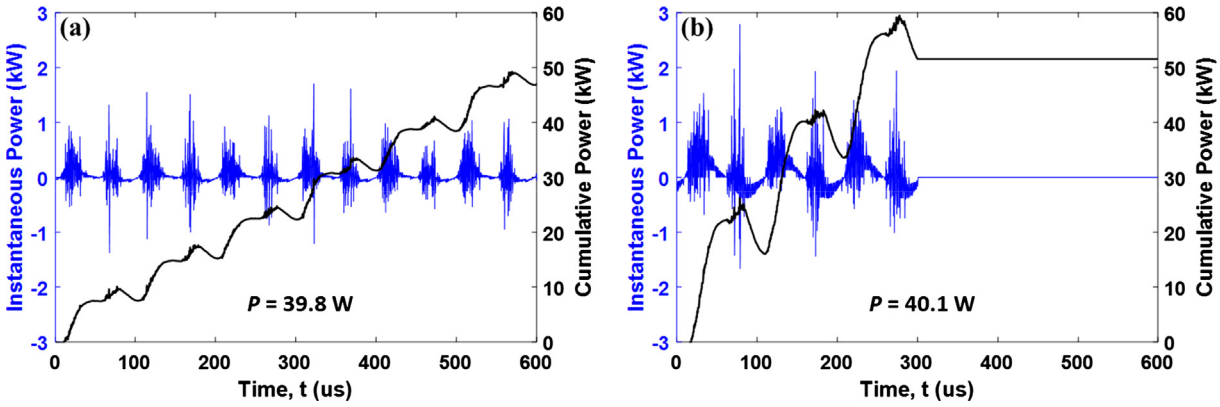

Fig. 5. Instantaneous and cumulative power of the AC-DBD plasma actuator in (a) the continuous mode and (b) duty-cycled mode (including both "on" and "off" periods in a complete cycle).

voltage and current input during the "on" period in the duty-cycle mode, the cumulative power is found to quickly increase over the "on" period, with a value being almost the same with that in the continuous plasma actuation over the whole cycle as shown in Fig. 5(b). As a result, the measured power is found to be almost the same between the continuous plasma actuation and the duty-cycled plasma actuation, i.e., P_0 = 39.8 W *vs.* P_1 = 40.1 W.

3.2. Thermal effects of DBD plasma actuation in the continuous mode and duty-cycled mode

As mentioned above, DBD plasma actuation can induce a strong thermal effect that has been utilized for anti-/de-icing applications [12]. It was suggested that the thermal energy in DBD plasma actuation is generated along with the formation of ionic airflow [42,43]. With the high-voltage signal applied to the exposed electrodes, a high-intensity electric field is generated between the exposed electrode and the grounded electrode separated by a dielectric layer. Driven by the electric field, the free electrons and ions in the air are responsible for energy transmission from the external power source to gas [42,44]. The free electrons get energy from the electric field through acceleration, and then collide with neutrals and ions in the air. If an elastic collision occurs, there is an immediate but only a small portion of total energy release, while in inelastic collisions, ionized particles and excited molecules can be produced, which are the main sources of energy heating the gas [44]. Collision between ions and neutrals/electrons is another source that contributes to the thermal energy generation in DBD plasma actuation [45]. A recent study by Rodrigues et al. [46] also revealed that the increase of input voltage to a DBD plasma actuator would result in a significant increase of thermal energy generation.

Fig. 6 shows the time-evolution of the measured surface temperature distribution over the airfoil model with the two arrays of plasma actuators being turned on simultaneously (i.e., duty-cycled plasma ($f_{duty\text{-}cycle}$ = 1 Hz) on the left side *vs.* continuous plasma actuation on the right side). The comparison was made under a dry test condition of U_∞ = 40 m/s, T_∞ = −5 °C and LWC = 0 g/m^3. To keep the power the same for the two arrays of the plasma actuators, i.e., $P_0 = P_1$ = 40 W, while the peak-to-peak voltage applied to the plasma actuators in the continuous mode was set at $V_{0\text{-}p\text{-}p}$ = 11.5 kV with a central frequency of f = 10 kHz, the input voltage to the plasma actuators in the duty-cycled mode was increased to $V_{1\text{-}p\text{-}p}$ = 14.0 kV with the same frequency of f = 10 kHz. It is clearly seen that, after the two sets of plasma actuators were switched on, the surface temperatures over the dielectric layer and the exposed electrodes started to increase as shown in Fig. 6(a). As the time goes by, t = 10.0 s, the surface temperature distribution showed an evident temperature increase around the exposed electrodes as indicated in Fig. 6(b). It should be noted that, the temperatures over the airfoil surface with the duty-cycled plasma actuation (i.e., left side of the airfoil model) increased much faster than that with the continuous plasma actuation (i.e., right side of the airfoil model), which was suggested to be caused by the higher input voltage to the duty-cycled plasma actuator [46]. Though there would be thermal energy loss due to heat transfer during the "off" periods in the duty-cycled plasma actuation, its amount was relatively small in comparison to the amount of the additional thermal energy generated at the increased input voltage to the plasma actuators. As the time goes by, i.e., from t = 20.0 s to t = 40.0 s, the temperature distributions on both sides were found to become stable as shown in Fig. 6(c) and (d), indicating that thermal equilibrium states were achieved over the two sides of the airfoil surface.

Based on the measured surface temperature distributions over the airfoil surface as shown in Fig. 6, the span-averaged temperature profiles along the airfoil chord at the different time instants (i.e., t = 1.0 s, 10.0 s, 20.0 s, and 40.0 s) were extracted and plotted in Fig. 7. The chordwise locations of the exposed/buried electrodes were also illustrated in the plot. As clearly shown in Fig. 7, the temperature profiles at the different time instances showed similar distribution patterns on both sides of the airfoil model (i.e., plasma actuation in the duty-cycled mode *vs.* plasma actuation in the continuous mode). While the temperature peaks are located at the edges of the exposed electrodes, the temperatures over the surfaces of the exposed electrodes are higher than those over the dielectric surfaces, which is essentially due to the difference in thermal conductivities of the electrodes and the dielectric layer [26]. By comparing the temperature profiles generated in the two modes of plasma actuation, it can be clearly seen that the surface temperatures around the plasma actuators increase much faster in the duty-cycled mode than those in the case of the continuous mode, i.e., while the maximum temperatures at the electrode edges of the plasma actuators were found to be increased from T_{surf} = −5 °C to 6 °C within 40 s in the duty-cycled actuation mode (i.e., as given in Fig. 7(a)), the maximum temperature was only increased to about T_{surf} = 1 °C after 40 s of operation in the continuous actuation mode (i.e., as given in Fig. 7(b)). The magnitude of surface temperature increase caused by the duty-cycled plasma actuation is found to be almost twice of that in the continuous plasma actuation, which is consistent with the ratio of instantaneous power applied to the two plasma actuators.

In order to further evaluate the thermal characteristics of the duty-cycled plasma actuation and the continuous plasma actuation under the dry test condition (i.e., U_∞ = 40 m/s, T_∞ = −5 °C and

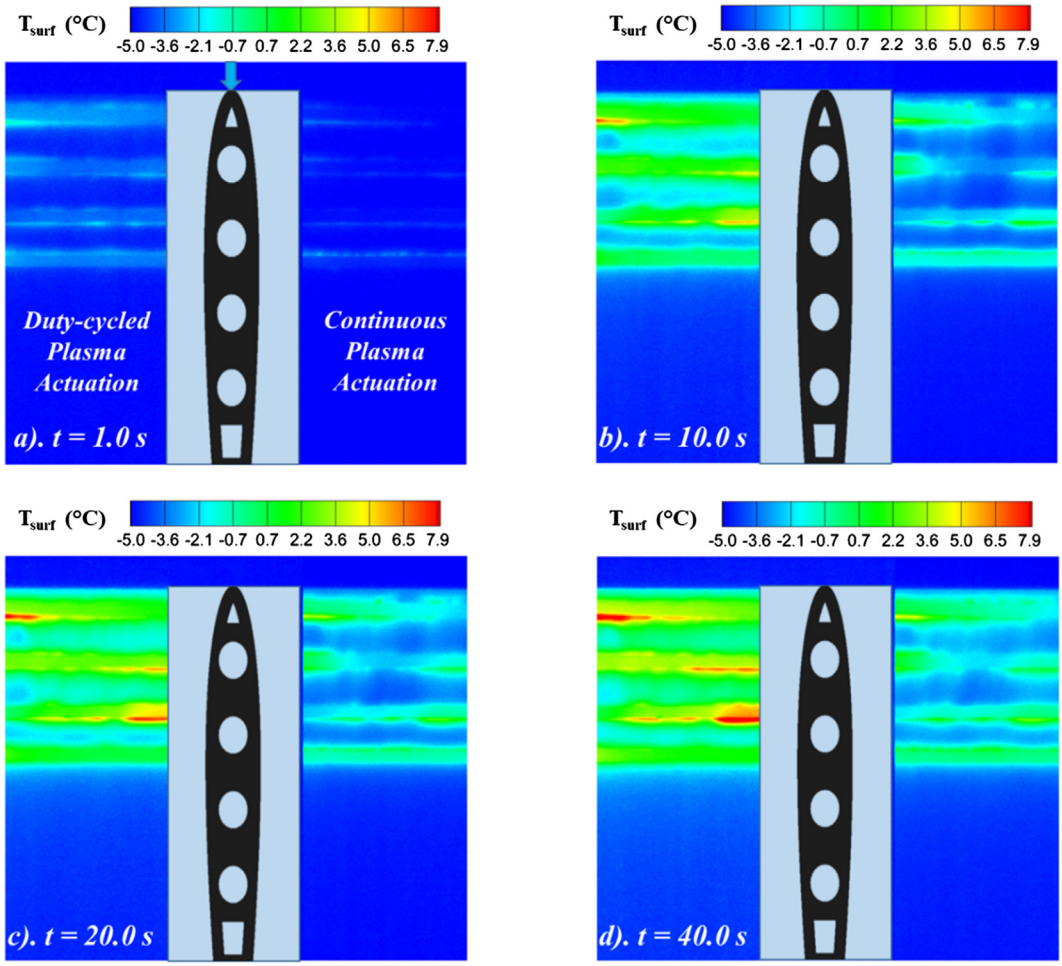

Fig. 6. Time-evolution of the measured surface temperature distribution over the airfoil model during the DBD plasma actuation with a power of $P = 40$ W (i.e., left: plasma actuation in the duty-cycled mode ($f_{duty\text{-}cycle} = 1$ Hz) *vs.* right: plasma actuation in the continuous mode) under a dry test condition of $U_\infty = 40$ m/s and $T_\infty = -5$°C.

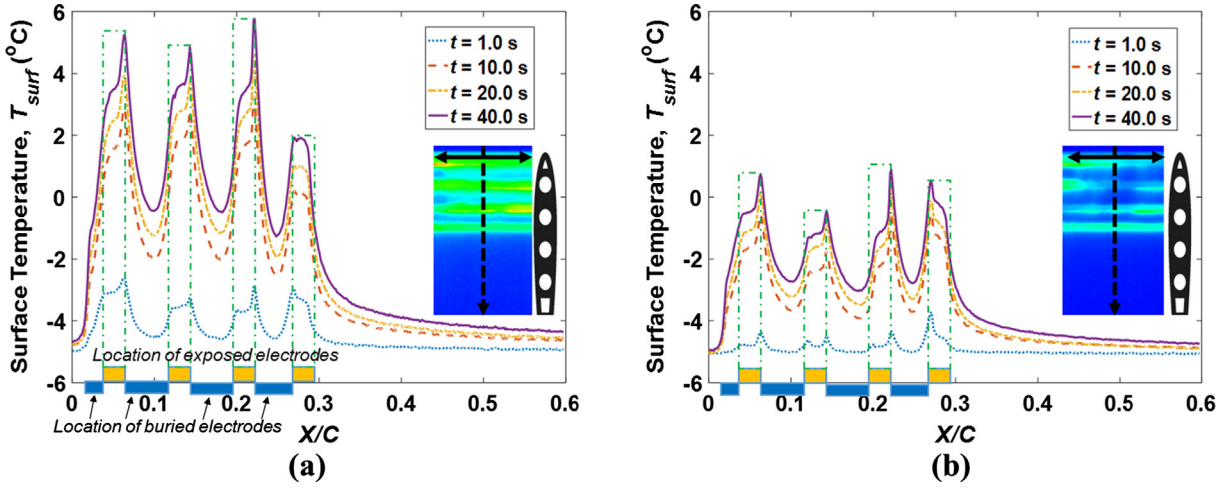

Fig. 7. The spanwise-averaged temperature profiles along the airfoil chord with the plasma actuators being operated at the power of $P = 40$ W, under a dry test condition of $U_\infty = 40$ m/s, $T_\infty = -5$ °C and $LWC = 0$ g/m^3. (a) Plasma actuation in the duty-cycled mode ($f_{duty\text{-}cycle} = 1$ Hz) at $V_{p\text{-}p} = 14$ kV, $f = 10$ kHz; (b) plasma actuation in the continuous mode at $V_{p\text{-}p} = 11.5$ kV, $f = 10$ kHz.

$LWC = 0$ g/m^3), the time-histories of the "span-averaged" surface temperature variations at different chordwise locations (i.e., location A at 2% chord, B at 10% chord, C at 18% chord, D at 25% chord, and E at 45% chord, as indicated in Fig. 8) on the two sides (i.e., the plasma actuation in the duty-cycled mode at $f_{duty\text{-}cycle} = 1$ Hz *vs.* the plasma actuation in the continuous mode) of the airfoil surface were also extracted as shown in Fig. 8. It is seen clearly that, while the temperature variations in the case of duty-cycled plasma

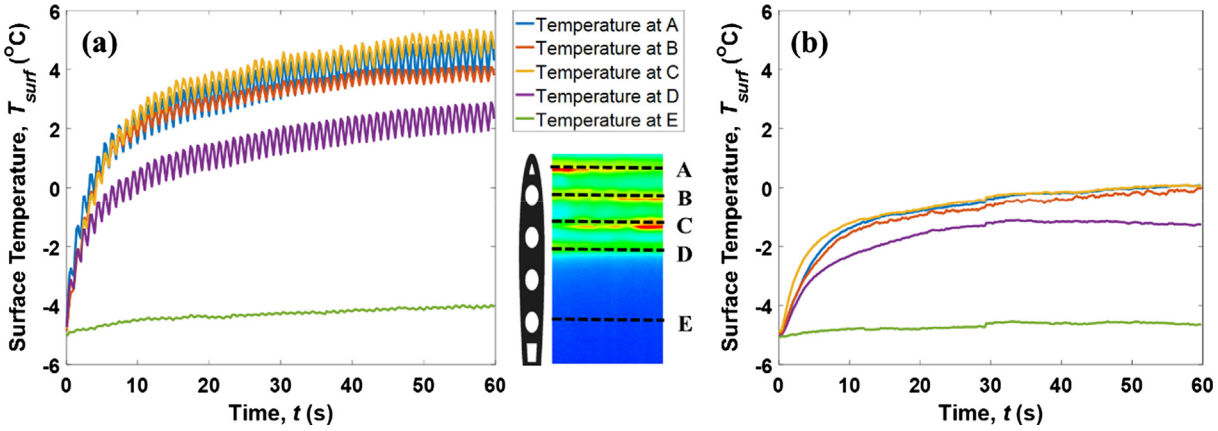

Fig. 8. Time-histories of the "span-averaged" surface temperature variations at different chordwise locations on the two sides of the airfoil model: (a) left side with the plasma actuation in the duty-cycled mode ($f_{duty\text{-}cycle}$ = 1 Hz) and (b) right side with the plasma actuation in the continuous mode, under a dry test condition of U_∞ = 40 m/s, T_∞ = −5°C and LWC = 0 g/m^3.

actuation show evident zigzag profiles as given in Fig. 8(a), the temperature profiles in the case of continuous plasma actuation are much smoother as shown in Fig. 8(b). For the duty-cycled plasma actuation in this case, since the modulating frequency of duty cycles is relatively low, $f_{duty\text{-}cycle}$ = 1 Hz, the time interval reserved for the heat transfer (i.e., convective and conductive heat transfer) to freely dissipate the thermal energy is relatively large, Δt = 0.5 s. During the "off" periods of the plasma actuation, while no additional thermal energy would be generated over the airfoil surface, the heat transfer can freely take away some of the remaining thermal energy, resulting in an obvious decrease of the local temperature. Once the plasma actuator is "on", a large amount of thermal energy would be generated immediately (which is much faster in comparison to the rate of heat transfer to take away the thermal energy), leading to a rapid temperature increase with a larger magnitude. Thus, zigzag profiles of the local temperature variations were formed during the alternate "on" and "off" cycles of the plasma actuation as shown in Fig. 8(a).

Along with the dynamic fluctuation of the local temperatures in the duty-cycled plasma actuation, the trends of the temperature evolutions at the different chordwise locations (i.e., A, B, C and D) are found to be very similar (i.e., the temperature increases first and becomes stable later) to those in the case of continuous plasma actuation. The "span-averaged" temperatures at the locations A, B, and C (where double-sided plasma discharge exists) are higher than that at the location D (where only one-side plasma discharge is accomplished). By comparing the temperature variations in the duty-cycled plasma actuation and the continuous plasma actuation, it can be found that while the surface temperature increases much faster in the duty-cycled plasma actuation, the temperature evolution trends at the corresponding locations are almost the same, which is essentially determined by the competing process between the rate of heat generation in plasma actuation and the rate of heat dissipation over the airfoil surface. As the time goes by, the surface temperature would increase due to the thermal energy generation, which in turn enhances the convective and conductive heat transfer attributing to the larger temperature difference between the surface and the airflow. Eventually, the rate of thermal energy generation and the rate of heat transfer would become equal with the surface temperatures becoming constant, which is called the thermal equilibrium state [26].

Fig. 9 shows the time-histories of the spatially-averaged temperature over the plasma region (i.e., as indicated by the red dashed rectangular in the temperature contour, ranging from the leading edge to 30% chord, in Fig. 9(a)) during the plasma actuations in the continuous mode and the duty-cycled modes with various modulating frequencies (i.e., $f_{duty\text{-}cycle}$ = 1 Hz, 5 Hz, 50 Hz, 100 Hz, and 200 Hz), under the same dry test condition (i.e., U_∞ = 40 m/s, T_∞ = −5 °C and LWC = 0 g/m^3). As can be seen clearly in Fig. 9(b), the trends of the temperature variations at the different plasma actuation modes are almost the same, with the temperature being increased quickly at first, and then gradually becoming constant as the time goes by. The temperature increases during the plasma actuation in the duty-cycled modes (at different modulating frequencies) are found to be obviously larger than that during the plasma actuation in the continuous mode (i.e., at least twice in amplitude), which is essentially due to the higher voltage input to the plasma actuator in the duty-cycled mode (during the "on" periods). It is also found that, as the modulating frequency increases, the surface temperature within the plasma region would increase faster and have a higher thermal equilibrium value as shown in Fig. 9(b). By zooming in the temperature variations within the first 2.5 s of plasma actuation as shown in Fig. 9(c), it is found that the temperature fluctuation would become much smaller at the higher modulating frequencies of duty cycles. For example, while the temperature variation at $f_{duty\text{-}cycle}$ = 1 Hz shows an obvious waveform with two and half cycles, the temperature profile at $f_{duty\text{-}cycle}$ = 5 Hz is found to have much smaller fluctuating amplitude but more cycles of the small waveform (about 12.5 cycles). As the modulating frequency of duty cycles further increases, i.e., $f_{duty\text{-}cycle}$ = 50 Hz, 100 Hz and 200 Hz, the temperature profiles are found to become much smoother with no evident waveform being observed.

As suggested by Tirumala et al. [42], the primary heating mechanism in plasma actuation is through heat transfer from the plasma to the ambient gas, which then heats up the dielectric/electrode surface through direct injection, convection and radiation. While the duty-cycled plasma actuation could create a train of co-rotating vortices, the size and vorticity of which are highly dependent on the duty cycle frequency [30], i.e., the increase of the modulating frequency of duty-cycled plasma actuation could result in the generation of smaller scale vortices with more concentrated vorticity located more closer to the surface [33] as clearly shown in Fig. 10. Since the larger vortices would lead to more heat convection from the heated gas layer to the mainstream, the increase of the modulating frequency of duty-cycled plasma actuation actually promotes the thermal energy attachment to the surface, with less heat being dissipated to the mainstream. As a result, the surface temperature would increase more at the higher duty cycle frequencies of the plasma actuation as shown in Fig. 9(b).

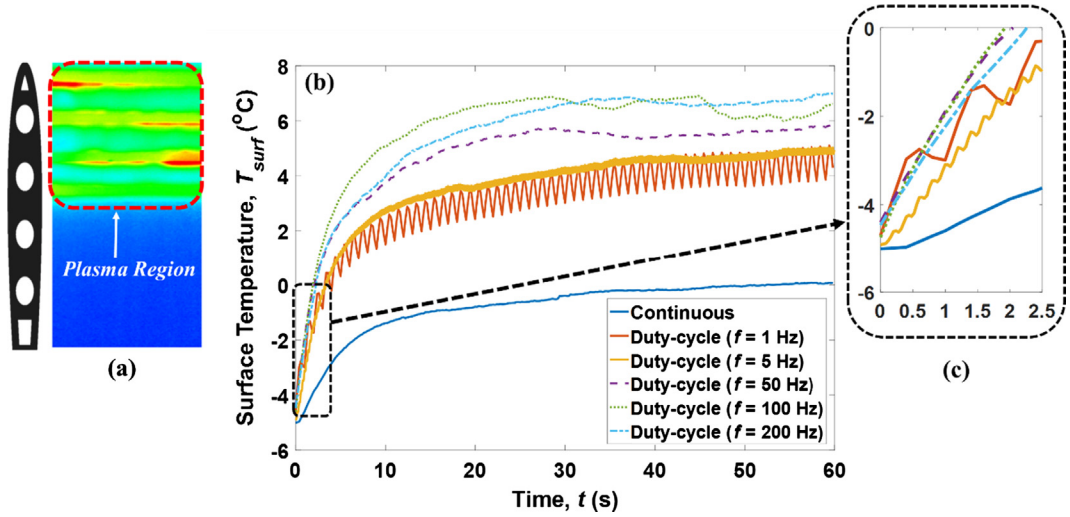

Fig. 9. Time-histories of the spatially-averaged temperature over the plasma region during the DBD plasma actuation in the continuous mode and the duty-cycled modes with different modulating frequencies (i.e., $f_{duty\text{-}cycle}$ = 1 Hz, 5 Hz, 50 Hz, 100 Hz, and 200 Hz), under a dry test condition of U_∞ = 40 m/s, T_∞ = −5°C and LWC = 0 g/m^3.

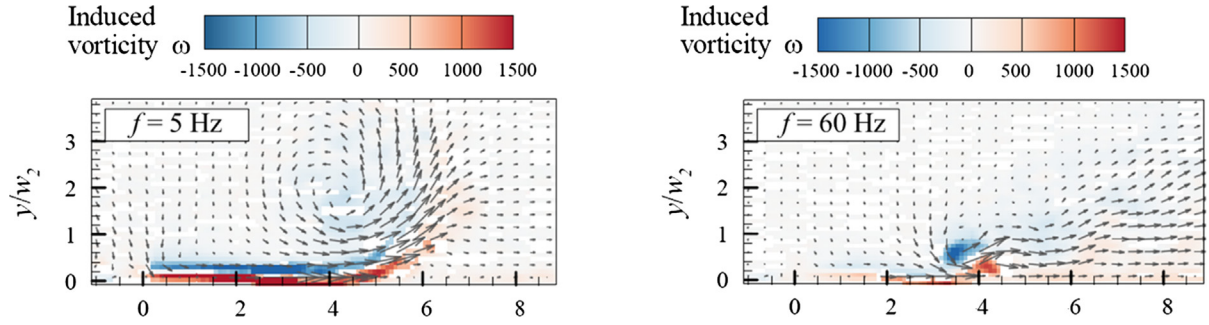

Fig. 10. Phased-locked vorticity field of duty-cycled DBD plasma actuation at $\phi = 12\pi/13$ with the duty-cycle frequencies being set at f = 5 Hz and 60 Hz [33].

3.3. Anti-/de-icing performances of the plasma actuators in the continuous mode and duty-cycled mode

In the present study, the ice accretion experiments were also performed on the airfoil model to evaluate the anti-/de-icing performances of the DBD plasma actuators in the two different actuation modes (i.e., in duty-cycled actuation mode *vs.* in conventional continuous actuation mode). Before the icing experiments were started, the ISU-IRT was first operated at a prescribed frozen-cold temperature level (e.g., T_∞ = −5 °C for the present study) for at least 60 min to ensure a thermal steady state within the ISU-IRT. Then, the AC-DBD plasma actuators embedded over the airfoil surface were switched on for about 60 s to achieve a thermal equilibrium state before turning on the water spray system of the ISU-IRT. The moment of switching on the water spray system was defined as $t = t_0$, after which the super-cooled water droplets would impinge onto the surface of the airfoil model to start the ice accretion process. During the icing experiments, the dynamic ice accretion process and the corresponding surface temperature evolution over the airfoil surface were recorded simultaneously by synchronizing the high-speed imaging system and the IR thermal imaging system. Figs. 11 and 12 give the time-evolutions of the dynamic ice accretion process and the corresponding surface temperature distributions over the airfoil surface embedded with the two arrays of DBD plasma actuators (i.e., the plasma actuator in the duty-cycled mode at $f_{duty\text{-}cycle}$ = 1 Hz on the left side *vs.* the plasma actuators in the continuous mode on the right side) being operated at the same power of P = 40 W. The box in red dashed lines in Fig. 11(a) indicates the measurement window of the IR thermal imaging system.

For the ice accretion process in this case, since the airfoil surface had been heated up before the ice accretion process was started, when the supercooled water droplets impinged onto the airfoil surface, the impinged water droplets would be instantly heated by absorbing the thermal energy generated in the plasma actuation. As can be seen clearly in Fig. 11(a), at the beginning stage of the ice accretion process, i.e., $t = t_0$ + 5.0 s, due to the warm surface of the airfoil model, the impinged water droplets were kept in the liquid state and transported downstream as driven by the boundary layer airflow. The corresponding temperature distribution of the airfoil surface is shown in Fig. 12(a). It can be found that while the temperature on the left side of the airfoil (i.e., with the duty-cycled plasma actuation) is obviously above the freezing point (i.e., T_{freeze} = 0 °C), the temperature distribution on the right side (i.e., with the continuous plasma actuation) is much lower, with the local temperature around the leading edge being subzero. As the time goes by, i.e., $t = t_0$ + 20.0 s, while the surface with the duty-cycled plasma actuation was still free of ice, an ice film was found to be formed over the surface with the continuous plasma actuation as shown in Fig. 11(b). It is suggested that the thermal energy generated in the duty-cycled plasma actuation was sufficient to keep the impinged water droplets warm and in the liquid state. However, for the continuous plasma actuation, though the power input was kept the same, the thermal energy generated in the plasma actuation was significantly reduced due to the lower voltage input to the plasma actuators. Thus, the thermal energy

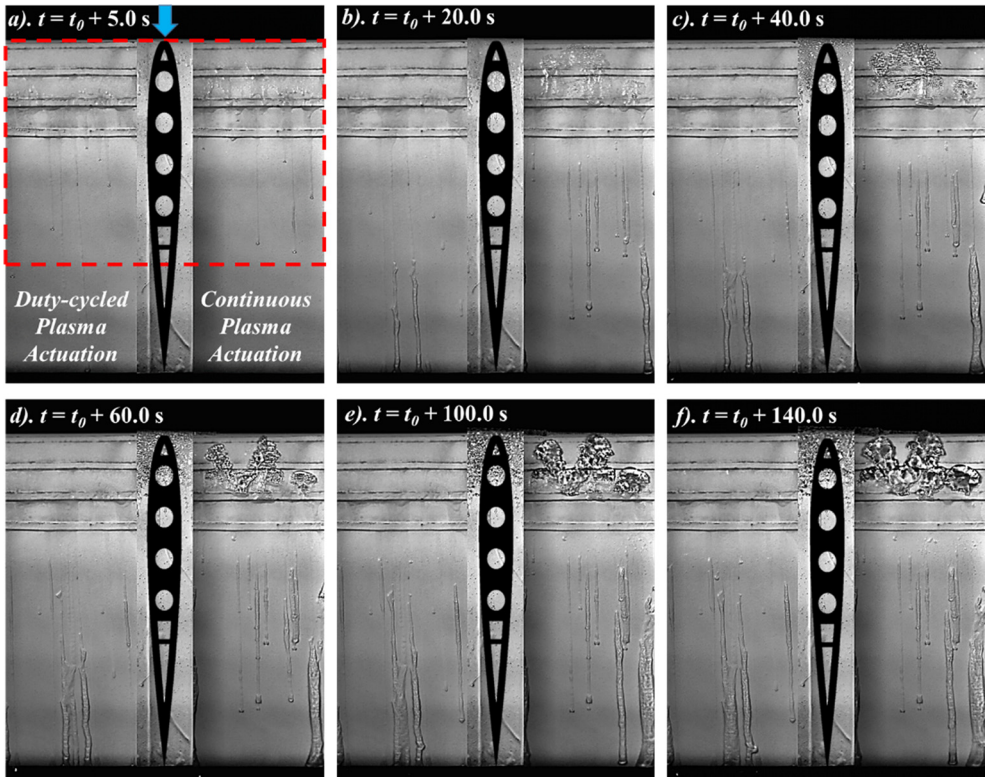

Fig. 11. Time-evolution of the dynamic ice accretion process over the airfoil surface (i.e., the plasma actuators in the duty-cycled mode ($f_{duty\text{-}cycle}$ = 1 Hz) on the left side *vs.* the plasma actuators in the continuous mode on the right side) under the icing condition of U_∞ = 40 m/s, T_∞ = −5 °C and *LWC* = 1.0 g/m^3.

generated over the plasma region was not enough to compensate the heat transfer and the energy requirement to keep the impinged water in the liquid state. As a result, the surface temperature around the leading edge was found to be below zero as shown in Fig. 12(b), leading to the formation of the ice film. As more and more super-cooled water droplets impinged onto the airfoil surface, while the plasma region on the left side (with duty-cycled plasma actuation) was always kept free of ice, the ice film formed on the right side (with continuous plasma actuation) was found to become thicker and thicker and grow into a large ice structure as shown in Fig. 11(c) to (f). It should be noted that, while the upstream icing morphologies were different on the two sides of the airfoil model, similar rivulets-shaped ice features were found to be formed in the downstream locations on both sides as shown in Fig. 11(b) to (f). The formation of these downstream ice features was essentially caused by the heat transfer (i.e., convective and conductive heat transfer) that can remove all of the latent heat of fusion in the surface water rivulets as they transported downstream [35].

Based on the corresponding temperature distributions given in Fig. 12, it can be found that the surface temperature distribution over the airfoil surface with the duty-cycled plasma actuation was always kept above zero throughout the dynamic ice accretion process. While most of the high-temperature spots were still located at the edges of the exposed electrodes, some "hot water" channels were also found to be formed over the dielectric surfaces between the exposed electrodes as clearly shown in Fig. 12(b). The formation of these "hot water" channels was suggested to be caused by the extended glow discharge at the edges of the surface water rivulets as they traveled through the gaps between the exposed electrodes [40]. As the time goes by, the further impinged water droplets were found to form into water films and flush over the plasma region showing a higher temperature distribution as shown in Fig. 12(c) to (f). Different from that in the duty-cycled plasma actuation, the temperature distribution on the right side (i.e., with the continuous plasma actuation) was found to only change slightly throughout the ice accretion process, with the temperature around the leading edge being kept below zero.

In the present study, various modulating frequencies of duty cycles (i.e., $f_{duty\text{-}cycle}$ = 1 Hz, 5 Hz, 50 Hz, 100 Hz, and 200 Hz) in the duty-cycled plasma actuation were tested in the ice accretion experiments to examine the effect of the modulating frequency of duty cycles on the anti-/de-icing performance of the DBD plasma actuation. Fig. 13 shows a comparison of the icing morphologies (after 140 s of ice accretion process) over the airfoil surfaces with different operational modes of the DBD plasma actuators. It is clearly seen that, the duty-cycled plasma actuation shows a much better anti-/de-icing performance (i.e., with the plasma region in upstream being completely free of ice) in comparison to that of the continuous plasma actuation. By comparing the icing morphologies formed at the different duty cycle frequencies, it can be found that along with the increase of the modulating frequency of duty cycles, less rivulets-shaped ice features would be formed in the downstream locations as shown in Fig. 13.

Fig. 14 shows the corresponding temperature distributions of the ice accreted airfoil surfaces given in Fig. 13. It can be found that while the surface temperature distributions in the cases of the duty-cycled plasma actuation are much higher than that in the case of continuous plasma actuation, the increase of the modulating frequency of duty cycles would further enhance the thermal effects of the duty-cycled plasma actuation, resulting in a higher temperature distribution over the plasma region as clearly shown in Fig. 14. The enhanced thermal effects induced in the duty-cycled plasma actuation at the higher modulating frequencies are

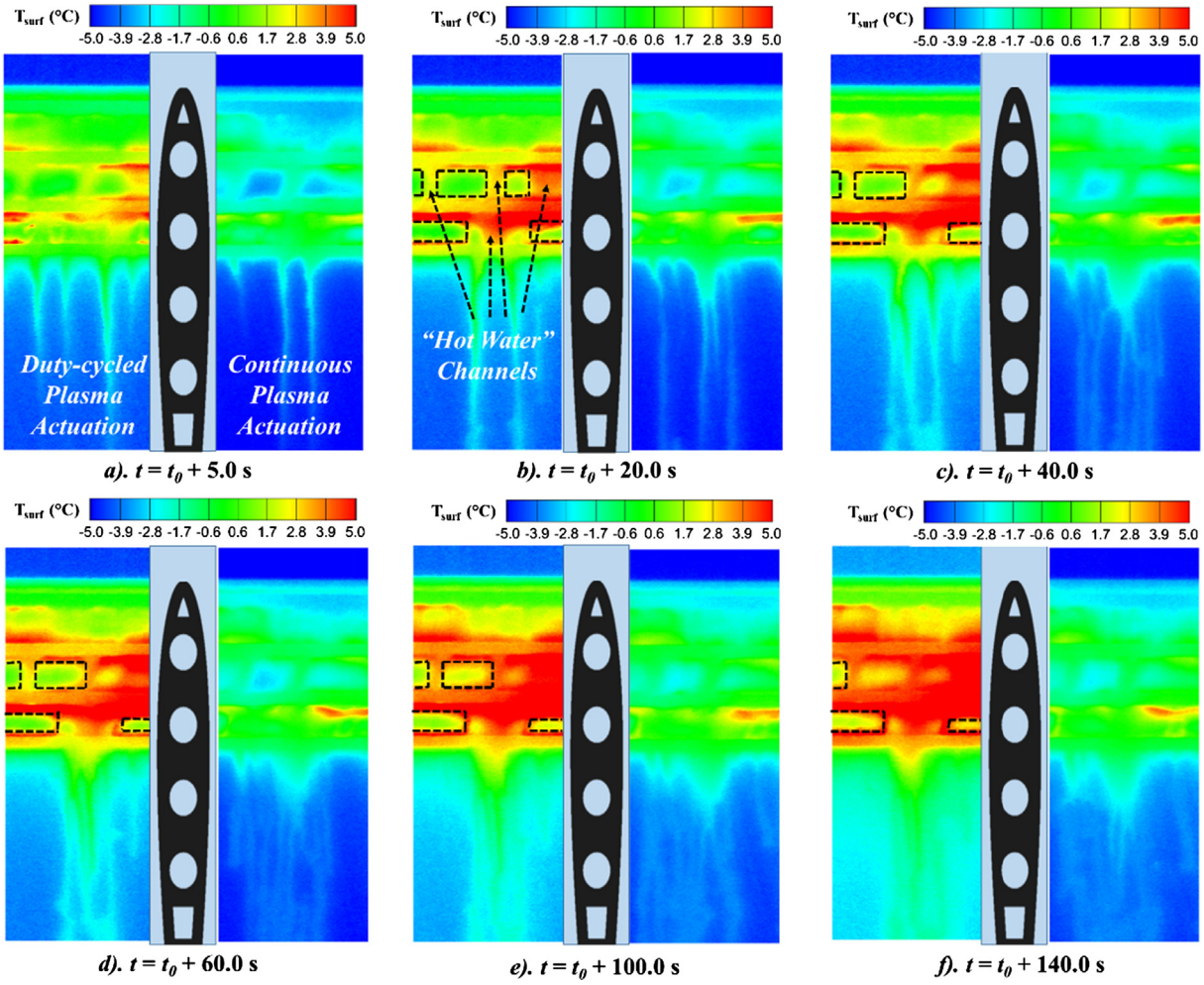

Fig. 12. Time-evolution of the temperature distributions over the airfoil surface (i.e., the plasma actuators in the duty-cycled mode on the left side *vs.* the plasma actuators in the continuous mode on the right side) with the same power of $P = 40$ W under the icing condition of $U_\infty = 40$ m/s, $T_\infty = -5$ °C and $LWC = 1.0$ g/m^3.

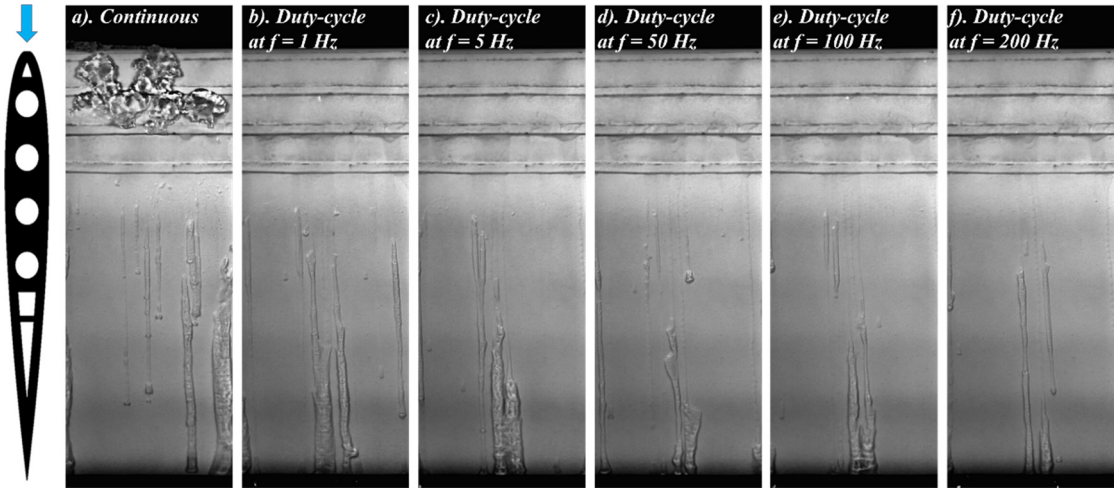

Fig. 13. Comparison of the icing morphologies (after 140 s of ice accretion process) over the airfoil surfaces with different operational modes of the DBD plasma actuators.

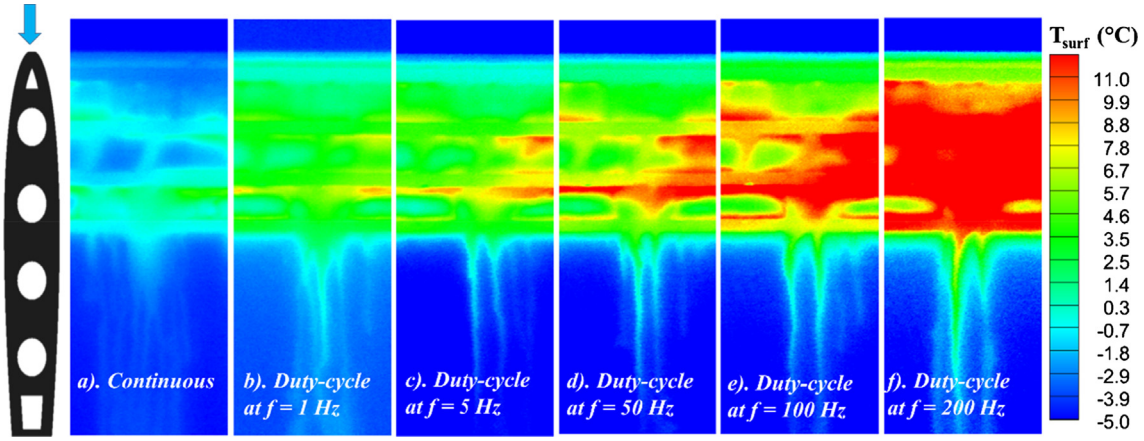

Fig. 14. Comparison of the surface temperature distributions over the ice accreted airfoil model (after 140 s of ice accretion process) with different operational modes of the DBD plasma actuators.

suggested to be very beneficial in improving the anti-/de-icing performance of AC-DBD plasma actuation to ensure the safer and more efficient aircraft operations in atmospheric icing conditions.

4. Conclusion

A comprehensive experimental study was performed to investigate the thermal effects induced by duty-cycled DBD plasma actuation for aircraft icing mitigation. A NACA0012 airfoil model embedded with DBD plasma actuators was placed in the unique Icing Research Tunnel available at Iowa State University (i.e., ISU-IRT) for the present study. During the experiments, the airfoil model was exposed in a typical glaze icing condition (i.e., freestream airflow velocity U_∞ = 40 m/s, LWC = 1.0 g/m^3, and airflow temperature of T_∞ = −5 °C), the DBD plasma actuators were operated in two different modes for quantitative comparison, i.e., in duty-cycled actuation mode *vs.* in conventional continuous actuation mode as the comparison baseline. The transient thermal characteristics induced by the DBD plasma actuations in two different actuation modes (i.e., duty-cycled actuation mode *vs.* conventional continuous actuation mode) were examined quantitatively based on the time-resolved surface temperature distributions acquired by using a high-speed infrared (IR) thermal imaging system. The anti-/de-icing performances of the DBD plasma actuators under different actuation modes were also evaluated base on the side-by-side comparisons of the snapshot images acquired by using a high-speed imaging system along with the synchronized IR thermal imaging results over the ice accreting airfoil surfaces. The effects of the modulating frequency of the duty-cycle actuation on the thermal effects of DBD plasma actuation as well as the resultant anti-/de-icing performances were also explored in this study.

It was found that, with the same power input, the plasma actuation in duty-cycled mode would have a much higher instantaneous voltage during the "on" periods of the cycles, in comparison to the case in the continuous actuation mode. Corresponding to the higher instantaneous voltage supplied to the DBD plasma actuators, much more thermal energy was found to be generated, as indicated by the higher surface temperature increases over the ice accreting airfoil surface for the case with the DBD plasma in duty-cycled actuation mode. The amount of thermal energy loss during the "off" periods of the duty-cycles was found to be rather small in comparison to the amount of the additional thermal energy generated at the increased instantaneous voltage input of the plasma actuator.

By extracting the time-histories of the measured surface temperature variations during the duty-cycled plasma actuations, evident zigzag features were observed in the temperature variation profiles for the test cases at low duty cycle frequencies (e.g., $f_{duty\text{-}cycle}$ = 1 Hz and 5 Hz). It indicates that, while some of the thermal energy can be freely dissipated by the heat transfer during the "off" periods of the actuation duty-cycles, a larger amount of thermal energy would be generated during the "on" periods of the duty-cycles, resulting in the zigzag features in the measured surface temperature profiles, corresponding to the alternate "on" and "off" cycles of the plasma actuation. It was also found that, as the modulating frequency of the duty cycle increases, the surface temperatures within the plasma actuation regions would increase faster and have higher temperature values at the thermal equilibrium state. This is believed to be caused by the generation of smaller vortices induced by the duty-cycled plasma actuation at higher duty-cycle frequencies with more thermal energy being concentrated along the surface (i.e., less heat being dissipated to the mainstream in comparison to that with larger vortex structures generated at lower duty-cycle frequencies), allowing more thermal energy to be used to heat up the dielectric/-electrode surfaces.

In the present study, the ice accretion experiments were also performed on the airfoil model to evaluate the anti-/de-icing performances of the different plasma actuation modes (i.e., duty-cycled plasma actuation *vs.* continuous plasma actuation). It was demonstrated clearly that, for the same airfoil model embedded with the same DBD plasm actuators, the anti-/de-icing performance of the DBD plasma actuators was found to vary significantly under different actuation modes (i.e., duty-cycled actuation mode *vs.* continuous actuation mode). With the same power input, the DBD plasma actuation in duty-cycled mode exhibited a much better anti-/de-icing performance, in comparison to that in continuous actuation mode. Since the thermal effects induced by the duty-cycled plasma actuation can be further enhanced by increasing of the modulating frequency of the duty cycles, it was utilized to further improve the anti-/de-icing performance of DBD plasma actuation. The findings derived from the present study could be used to explore/optimize design paradigm for the development of novel DBD-plasma-based anti-/de-icing strategies tailored specifically for aircraft icing mitigation.

Acknowledgments

The research work is partially supported by Iowa Space Grant Consortium (ISGC) Base Program for Aircraft Icing Studies and National Science Foundation (NSF) under award numbers of CMMI-1824840 and CBET-1435590.

Appendix A. Supplementary material

Supplementary data to this article can be found online at https://doi.org/10.1016/j.ijheatmasstransfer.2019.03.068.

References

[1] T. Cebeci, F. Kafyeke, Aircraft icing, Annu. Rev. Fluid Mech. 35 (2003) 11–21.
[2] M.B. Bragg, A.P. Broeren, L.A. Blumenthal, Iced-airfoil aerodynamics, Prog. Aerosp. Sci. 41 (2005) 323–362, https://doi.org/10.1016/j.paerosci.2005.07.001.
[3] R.J. Hansman, M.S. Kirby, Comparison of wet and dry growth in artificial and flight icing conditions, J. Thermophys. Heat Transfer 1 (1987) 215–221.
[4] S.E. Campbell, A.P. Broeren, M.B. Bragg, Sensitivity of aircraft performance to icing parameter variations, J. Aircr. 44 (2007) 1758–1760, https://doi.org/10.2514/1.32355.
[5] Y. Liu, L.J. Bond, H. Hu, Ultrasonic-attenuation-based technique for ice characterization pertinent to aircraft icing phenomena, AIAA J. 55 (2017) 1–8, https://doi.org/10.2514/1.J055500.
[6] Y. Liu, L. Li, Z. Ning, W. Tian, H. Hu, Experimental investigation on the dynamic icing process over a rotating propeller model, J. Propuls. Power. (2018) 1–15, https://doi.org/10.2514/1.B36748.
[7] M.K. Politovich, Aircraft icing caused by large supercooled droplets, J. Appl. Meteorol. 28 (1989) 856–868, https://doi.org/10.1175/1520-0450(1989)028<0856:AICBLS>2.0.CO;2.
[8] M. Bragg, G. Gregorek, J. Lee, Airfoil aerodynamics in icing conditions, J. Aircr. 23 (1986) 76–81.
[9] G. Momen, R. Jafari, M. Farzaneh, Ice repellency behaviour of superhydrophobic surfaces: effects of atmospheric icing conditions and surface roughness, Appl. Surf. Sci. 349 (2015) 211–218, https://doi.org/10.1016/j.apsusc.2015.04.180.
[10] M. Pourbagian, W.G. Habashi, Aero-thermal optimization of in-flight electro-thermal ice protection systems in transient de-icing mode, Int. J. Heat Fluid Flow. 54 (2015) 167–182, https://doi.org/10.1016/j.ijheatfluidflow.2015.05.012.
[11] Y. Liu, L. Li, H. Li, H. Hu, An experimental study of surface wettability effects on dynamic ice accretion process over an UAS propeller model, Aerosp. Sci. Technol. 73 (2018) 164–172, https://doi.org/10.1016/j.ast.2017.12.003.
[12] W. Zhou, Y. Liu, H. Hu, H. Hu, X. Meng, Utilization of thermal effect induced by plasma generation for aircraft icing mitigation, AIAA J. 56 (2018) 1097–1104, https://doi.org/10.2514/1.J056358.
[13] Y. Liu, L. Ma, W. Wang, A.K. Kota, H. Hu, An experimental study on soft PDMS materials for aircraft icing mitigation, Appl. Surf. Sci. 447 (2018) 599–609, https://doi.org/10.1016/J.APSUSC.2018.04.032.
[14] A. Overmeyer, J. Palacios, E. Smith, Ultrasonic de-icing bondline design and rotor ice testing, AIAA J. 51 (2013) 2965–2976, https://doi.org/10.2514/1.J052601.
[15] D.M. Ramakrishna, T. Viraraghavan, Environmental impact of chemical deicers – a review, Water. Air. Soil Pollut. 166 (2005) 49–63, https://doi.org/10.1007/s11270-005-8265-9.
[16] S.K. Thomas, R.P. Cassoni, C.D. MacArthur, Aircraft anti-icing and de-icing techniques and modeling, J. Aircr. 33 (1996) 841–854, https://doi.org/10.2514/3.47027.
[17] O. Parent, A. Ilinca, Anti-icing and de-icing techniques for wind turbines: critical review, Cold Reg. Sci. Technol. 65 (2011) 88–96, https://doi.org/10.1016/j.coldregions.2010.01.005.
[18] C. Antonini, M. Innocenti, T. Horn, M. Marengo, A. Amirfazli, Understanding the effect of superhydrophobic coatings on energy reduction in anti-icing systems, Cold Reg. Sci. Technol. 67 (2011) 58–67, https://doi.org/10.1016/j.coldregions.2011.02.006.
[19] L. Cao, A.K. Jones, V.K. Sikka, J. Wu, D. Gao, Anti-icing superhydrophobic coatings, Langmuir 25 (2009) 12444–12448, https://doi.org/10.1021/la902882b.
[20] K. Golovin, S.P.R. Kobaku, D.H. Lee, E.T. DiLoreto, J.M. Mabry, A. Tuteja, Designing durable icephobic surfaces, Sci. Adv. 2 (2016), https://doi.org/10.1126/sciadv.1501496, e1501496-e1501496.
[21] H. Sojoudi, M. Wang, N.D. Boscher, G.H. McKinley, K.K. Gleason, Z.Z. Yang, G.H. McKinley, K.K. Gleason, F. Liu, M.L. Hu, S.R. Hunter, J.A. Haynes, K.K. Gleason, Durable and scalable icephobic surfaces: similarities and distinctions from superhydrophobic surfaces, Soft Matter 12 (2016) 1938–1963, https://doi.org/10.1039/C5SM02295A.
[22] D.L. Beemer, W. Wang, A.K. Kota, M. Doi, F. Brochard-Wyart, A. Tuteja, J. Aizenberg, J. Wang, Y. Song, L. Jiang, Durable gels with ultra-low adhesion to ice, J. Mater. Chem. A 4 (2016) 18253–18258, https://doi.org/10.1039/c6ta07262c.
[23] O. Fakorede, H. Ibrahim, A. Ilinca, J. Perron, Experimental investigation of power requirements for wind turbines electrothermal anti-icing systems, in: Wind Turbines - Des. Control Appl., 2016, https://doi.org/10.5772/63449.
[24] W. Dong, J. Zhu, M. Zheng, Y. Chen, Thermal analysis and testing of nonrotating cone with hot-air anti-icing system, J. Propuls Power (2015) 1–8, https://doi.org/10.2514/1.B35378.
[25] J.-J. Wang, K.-S. Choi, L.-H. Feng, T.N. Jukes, R.D. Whalley, Recent developments in DBD plasma flow control, Prog. Aerosp. Sci. 62 (2013) 52–78, https://doi.org/10.1016/J.PAEROSCI.2013.05.003.
[26] Y. Liu, C. Kolbakir, H. Hu, H. Hu, A comparison study on the thermal effects in DBD plasma actuation and electrical heating for aircraft icing mitigation, Int. J. Heat Mass Transfer 124 (2018) 319–330, https://doi.org/10.1016/J.IJHEATMASSTRANSFER.2018.03.076.
[27] T.C. Corke, C.L. Enloe, S.P. Wilkinson, Dielectric barrier discharge plasma actuators for flow control, Annu. Rev. Fluid Mech. 42 (2010) 505–529, https://doi.org/10.1146/annurev-fluid-121108-145550.
[28] J. Cai, Y. Tian, X. Meng, X. Han, D. Zhang, H. Hu, An experimental study of icing control using DBD plasma actuator, Exp. Fluids 58 (2017) 102, https://doi.org/10.1007/s00348-017-2378-y.
[29] C.A. Borghi, A. Cristofolini, G. Neretti, P. Seri, A. Rossetti, A. Talamelli, Duty cycle and directional jet effects of a plasma actuator on the flow control around a NACA0015 airfoil, Meccanica 52 (2017) 3661–3674, https://doi.org/10.1007/s11012-017-0692-3.
[30] J.A. Vernet, R. Örlü, P.H. Alfredsson, Flow separation control by dielectric barrier discharge plasma actuation via pulsed momentum injection, AIP Adv. 8 (2018) 75229, https://doi.org/10.1063/1.5037770.
[31] M. Sun, B. Yang, T. Peng, M. Lei, Optimum duty cycle of unsteady plasma aerodynamic actuation for NACA0015 airfoil stall separation control, Plasma Sci. Technol. 18 (2016) 680–685, https://doi.org/10.1088/1009-0630/18/6/16.
[32] X. Meng, H. Hu, X. Yan, F. Liu, S. Luo, Lift improvements using duty-cycled plasma actuation at low Reynolds numbers, Aerosp. Sci. Technol. 72 (2018) 123–133, https://doi.org/10.1016/J.AST.2017.10.038.
[33] Y. Long, H. Li, X. Meng, J. Li, Z. Xiang, Structure optimization of the AC-SDBD plasma actuator under duty-cycle mode, Mod. Phys. Lett. B 32 (2018) 1850315, https://doi.org/10.1142/S0217984918503153.
[34] R.M. Waldman, H. Hu, High-speed imaging to quantify transient ice accretion process over an airfoil, J. Aircr. 53 (2015) 369–377, https://doi.org/10.2514/1.C033367.
[35] Y. Liu, H. Hu, An experimental investigation on the unsteady heat transfer process over an ice accreting airfoil surface, Int. J. Heat Mass Transfer 122 (2018) 707–718, https://doi.org/10.1016/j.ijheatmasstransfer.2018.02.023.
[36] Li. Li, H. Hu, An experimental study of dynamic ice accretion process on aero-engine spinners, in: 55th AIAA Aerosp. Sci. Meet., American Institute of Aeronautics and Astronautics, 2017, https://doi.org/10.2514/6.2017-0551.
[37] S.M. Soloff, R.J. Adrian, Z.-C. Liu, Distortion compensation for generalized stereoscopic particle image velocimetry, Meas. Sci. Technol. 8 (1997) 1441–1454, https://doi.org/10.1088/0957-0233/8/12/008.
[38] R. Joussot, V. Lago, J.-D. Parisse, Quantification of the effect of surface heating on shock wave modification by a plasma actuator in a low-density supersonic flow over a flat plate, Exp. Fluids 56 (2015) 102, https://doi.org/10.1007/s00348-015-1970-2.
[39] N. Benard, E. Moreau, Electrical and mechanical characteristics of surface AC dielectric barrier discharge plasma actuators applied to airflow control, Exp. Fluids 55 (2014) 1846, https://doi.org/10.1007/s00348-014-1846-x.
[40] S.B. Leonov, V. Petrishchev, I.V. Adamovich, Dynamics of energy coupling and thermalization in barrier discharges over dielectric and weakly conducting surfaces on μ s to ms time scales, J. Phys. D. Appl. Phys. 47 (2014) 465201, https://doi.org/10.1088/0022-3727/47/46/465201.
[41] D. Ashpis, M. Laun, E. Griebeler, Progress toward accurate measurements of power consumption of DBD plasma actuators, in: 50th AIAA Aerosp. Sci. Meet. Incl. New Horizons Forum Aerosp. Expo., American Institute of Aeronautics and Astronautics, Reston, Virigina, 2012, https://doi.org/10.2514/6.2012-823.
[42] R. Tirumala, N. Benard, E. Moreau, M. Fenot, G. Lalizel, E. Dorignac, Temperature characterization of dielectric barrier discharge actuators: influence of electrical and geometric parameters, J. Phys. D. Appl. Phys. 47 (2014), https://doi.org/10.1088/0022-3727/47/25/255203 255203.
[43] R. Joussot, V. Boucinha, R. Weber-Rozenbaum, H. Rabat, A. Leroy-Chesneau, D. Hong, Thermal characterization of a DBD plasma actuator: dielectric temperature measurements using infrared thermography, in: 40th Fluid Dyn. Conf. Exhib., American Institute of Aeronautics and Astronautics, Reston, Virigina, 2010, https://doi.org/10.2514/6.2010-5102.
[44] Y. Zhu, Y. Wu, W. Cui, Y. Li, M. Jia, Numerical investigation of energy transfer for fast gas heating in an atmospheric nanosecond-pulsed DBD under different negative slopes, J. Phys. D. Appl. Phys. 46 (2013) 495205, https://doi.org/10.1088/0022-3727/46/49/495205.
[45] H. Conrads, M. Schmidt, Plasma generation and plasma sources, Plasma Sources Sci. Technol. 9 (2000) 441–454, https://doi.org/10.1088/0963-0252/9/4/301.
[46] F. Rodrigues, J. Páscoa, M. Trancossi, Experimental analysis of DBD plasma actuators thermal characteristics under external flow influence, J. Heat Transfer. (n.d.). doi:10.1115/1.4040152.